



INDIAN INSTITUTE OF TECHNOLOGY BOMBAY

DEPARTMENT OF METALLURGICAL ENGINEERING & MATERIALS SCIENCE

Chiral Gold Nanomaterials for Photodetection Applications

BTech Project I

DANIEL GRACIAS

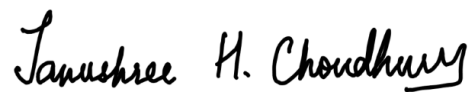
Under the guidance of
Prof. TANUSHREE CHOUDHURY

April, 2023

Department of Metallurgical Engineering and Materials Science
Indian Institute of Technology Bombay

The B-Tech project report entitled CHIRAL GOLD NANOMATERIALS FOR PHOTODETECTION APPLICATIONS submitted by Mr. Daniel Joel Gracias (Roll No. 200110029) may be accepted for being evaluated.

Date: 12th April 2023

A handwritten signature in black ink, reading "Tanushree H. Choudhury". The signature is written in a cursive style with a horizontal line under the last part of the name.

(Signature)
Prof Tanushree Choudhury

Abstract

Gold nanoparticles offer the potential to increase the sensitivity and range of detection of photodetectors by virtue of the phenomenon of local surface plasmon resonance. Moreover, introducing a chiral morphology results in the structure interacting differently with right-handed and left-handed circular polarized light. These effects allow for the construction of compact circular polarized light detectors, which have applications in bio-sensing and information transmission. One promising method for synthesizing such chiral nanomaterials is the seed-mediated synthesis, a simple solution-state process. The morphology and size of the nanoparticles can be kinetically controlled by fine-tuning the concentrations of the reagents. This study gives an overview of local surface plasmon resonance and seed-mediated synthesis. Finite element simulations in Lumerical FDTD are carried out to determine the dependence of the optical response of the nanoparticles on various parameters such as size, orientation with respect to incident light, and background refractive index. These simulations aim to understand and optimize relevant parameters, which will be implemented into the device architecture. Details of the experimental procedure I have followed to synthesize gold nanoparticles are also included.

Acknowledgements

I would like to express my gratitude to Prof. Revathy Padmanabhan for providing me with much-needed guidance for FDTD simulations in Lumerical. I would also like to thank Prof. Parag Bhargava for allowing me access to the equipment in his lab. Special thanks to Jeeta Ghosh for guiding me in synthesis.

Contents

Introduction	6
1 Local Surface Plasmon Resonances in Metals	7
1.1 Qualitative Picture	7
1.2 Drude Model	9
1.3 Quasistatic Approximation	9
2 Simulations	12
2.1 Spherical Nanoparticles	13
2.2 Octahedral Nanoparticles	14
2.3 Helicoidal Particles	18
3 Synthesis	25
3.1 Literature Review	25
3.2 Experimental Work	28

List of Figures

1.1 (a) Variation of colour of gold colloid with particle size [22] (b) Schematic of near-field coupling in a 1D array of metallic nanoparticles for the two different polarizations. In the first case the restoring force is increased, leading to a blueshift in the resonance frequency while in the second case there is a reduction in the restoring force leading to a redshift. [18]	8
1.2 Schematic of LSPR in nanospheres (top) [19] and nanorods (bottom) [4]	8
1.3 Quasistatic Approximation. [18]	10
2.1 Dielectric constant data used for simulations	13
2.2 Schematic of simulation setup and perspective view of setup in Lumerical	14
2.3 Variation of Absorption and Scattering with sphere diameter	15
2.4 Variation of Absorption and Scattering with refractive index	15
2.5 Simulation setup and definition of coordinate system (wave propagation is into the plane)	16
2.6 Variation of Absorption and Scattering with octahedron size	16
2.7 Variation of Absorption and Scattering with octahedron inclination to defined x-axis	17

2.8	Variation of Absorption and Scattering with octahedron inclination to defined z-axis	17
2.9	Plasmonic field intensification of octahedron nanoparticles at the mid-plane perpendicular to the direction of propagation corresponding to wavelengths 300nm (top) and 561nm (bottom)	18
2.10	Monte-Carlo Simulations corresponding to varying orientation	19
2.11	Average absorption and scattering results from Monte Carlo Simulations	20
2.12	CAD of Helicoid created in SolidWorks (left) and setup of geometry in Lumerical (right)	20
2.13	Circular Dichroism simulation of helicoidal nanoparticle in periodic array	22
2.14	Plasmonic field intensification at face of helicoid perpendicular to incident light at 627nm	22
2.15	Variation of Mie Absorption Efficiency (left) and Mie Scattering (right) with change in particles size. The simulated data is compared with built in function mie3d for comparison.	24
3.1	Ball models of FCC (643) and $(\overline{6}43)$ surfaces with step edges highlighted. The dotted line represents a mirror plane. [28]	27
3.2	Evolution of space groups with mirror symmetries into chiral space groups [21]	28
3.3	(left to right) Seed Solution, Growth Solution A, Growth Solution B as synthesized	29

Introduction

Metal nanostructures have attracted considerable attention both fundamentally and technologically because of their unique physical and chemical properties and functionalities compared to their bulk counterparts. Of these, their ability to sustain resonant oscillations of conduction electrons in response to electromagnetic waves is particularly interesting. This phenomenon is known as 'Localized Surface Plasmon Resonance (LSPR)'. LSPR leads to significant field intensification in the vicinity of the nanoparticles as well as an increase in absorption, which have tremendous potential in a wide variety of applications. These include bio-imaging, catalysis, photodetection and photovoltaics, radiation therapy and spectroscopy. Noble metals such as gold, silver and copper having high conductivities are generally used in these applications. This study will focus on the optical applications of metal nanoparticles, specifically gold nanoparticles in photodetection.

Photodetection can be plasmonically enhanced by two mechanisms, the first of which is the aforementioned field intensification. This leads to the intensification of weak EM waves, leading to an increase in the sensitivity of such photodetectors. The other mechanism involves hot electrons, which are generated via the enhanced absorption due to LSPR. If the metal nanostructures are in contact with a semiconductor, a Schottky junction will be formed allowing for the hot electron to be injected into the semiconductor, generating a current. This allows for detection of EM waves having energy well below the band gap of the semiconductor [16]. Thus implementing metal nanoparticles can augment both the sensitivity as well as the range of photodetection. Introducing chirality to the nanoparticle enables the nanoparticle to have a different plasmonic interaction with right handed and left handed circularly polarized light. This leads to the ability to detect the handedness of circular polarization of light using extremely compact components, and hence have potential in bio-sensing as well as transmitting information.

For synthesizing such chiral nanostructures, the seed mediated synthesis is a good candidate methodology. This solution state synthesis pathway allows for a fine tunability of the shape of the nanoparticle by splitting the nucleation and growth steps. It is a quick and simple method, and does not involve any complicated equipment. Moreover, it also allows for the potential of scalability [35]. Hence this pathway has been selected for analysis in this study. Specifically, this study aims to synthesize a Helicoid 432 III geometry following previous literature [5] as a preliminary step. In this article, gold nano-helicoids are synthesized from nano-octahedra.

Section 1 deals with an overview of the theory behind LSPR applicable to application of interest. Section 2 includes FDTD simulations carried out with an aim of understanding and optimizing relevant parameters. The 3rd section explains the seed-mediated synthesis pathway and the various factors involved, and also covers some of my own experimental work conducted so far as well as future goals.

1

Local Surface Plasmon Resonances in Metals

1.1 Qualitative Picture

When an electromagnetic wave is incident on a metal nanoparticle, it sets the conducting electrons within the metal into oscillation. The displaced electrons experience a restoring force from their Coulombic interactions with the positive ions as well as the other electrons. When the natural frequency of this displacement dependent restoring force matches the frequency of the incident EM wave, then the two are in phase and resonance takes place, which is termed as Local Surface Plasmon Resonance (LSPR). This phenomenon leads to a significant increase in the amplitude of the polarization, which in turn causes amplified local fields, higher absorption as well as scattering at the resonant frequency. For example, absorption at this resonant frequency is the source of the bright characteristic colours exhibited by gold nanoparticle colloids. The resonant modes correspond to standing waves of charge distributions on the surface of the nanoparticle. The fundamental mode corresponds to a dipole formed at the fundamental mode. Higher order multipoles can exist for higher frequencies and larger geometries. In general, only the fundamental mode is observed in the visible range. It should be noted that the LSPR phenomenon only takes place in structures having one or more dimensions significantly smaller than the wavelength of light. This ensures that there is negligible difference in the phases of the oscillating electrons, while also ensuring the amplitude of the oscillations is small enough[24]

Apart from the material properties of the metal, the LSPR frequencies depend on the size, shape and refractive index of the surrounding medium. Increasing the size of the nanoparticle allows for the electrons to travel a longer path before encountering a boundary, thus increasing the amplitude of resonant oscillations and reducing the resonance frequency. Thus gold colloids having larger (smaller) particles absorb longer (shorter) wavelengths, appearing purple (red) (Fig 1.1). Non spherical nanoparticles can support two or more distinct modes depending their geometry. This is due to the fact that electrons being oscillated in different directions will experience different boundaries, each corresponding to their own resonant frequencies. For example, nanorods support two dipole modes, one along the longer dimension and one along the shorter dimension, depending on the direction of incident field Fig 1.2. This leads to the presence of two distinct resonant frequencies. Hence colloids of gold nanorods have a resonant absorption at two different frequencies, leading to a broad spectrum

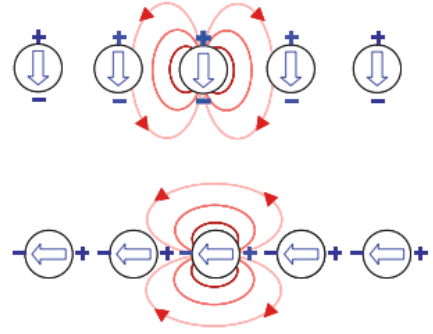
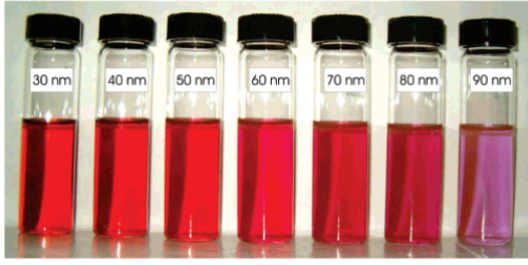


Figure 1.1: (a) Variation of colour of gold colloid with particle size [22] (b) Schematic of near-field coupling in a 1D array of metallic nanoparticles for the two different polarizations. In the first case the restoring force is increased, leading to a blueshift in the resonance frequency while in the second case there is a reduction in the restoring force leading to a redshift.[18]

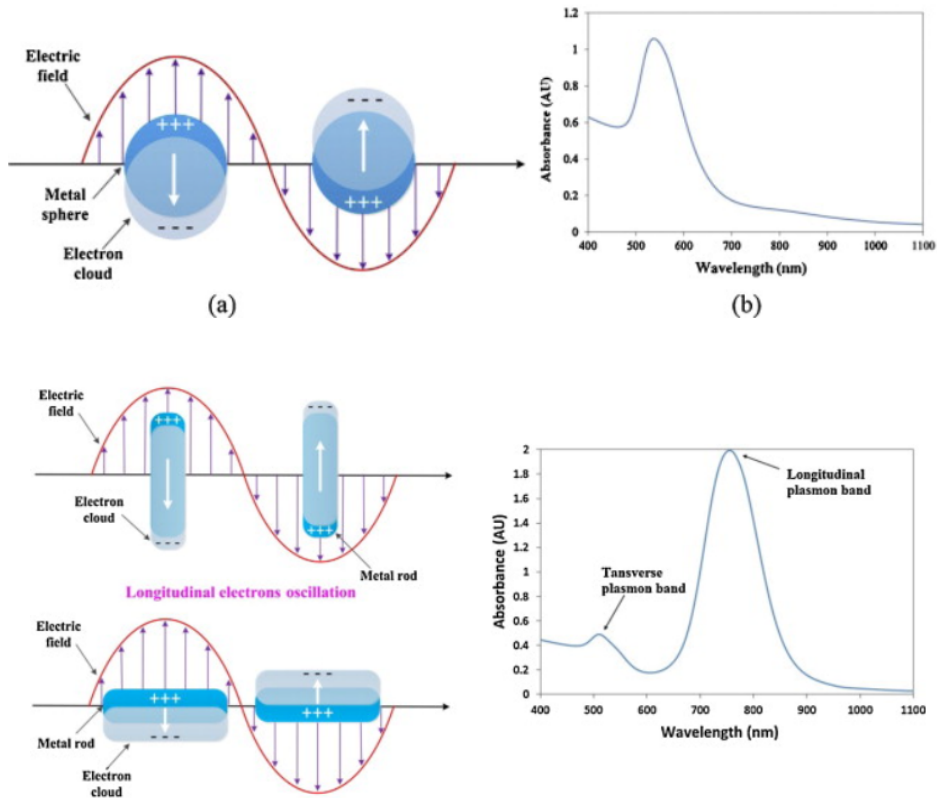


Figure 1.2: Schematic of LSPR in nanospheres (top) [19] and nanorods (bottom) [4]

of colours depending on their size and aspect ratio. The dependence of resonance frequency on refractive index leads to applications in refractive index sensing. LSPRs can also exhibit near-field coupling between different particles at a close proximity ($d \ll \lambda$) as shown in Fig. 1.1 [18].

1.2 Drude Model

Metal nanoparticles are big enough for classical theories to be able to sufficiently quantify their behaviour. Thus Maxwell's equations (and by extension, the Laplace equation) are able to obtain sufficiently accurate results. Since this analysis deals with noble metals, the Drude model is a valid approximation of the electronic behaviour. Consider a conduction electron displaced by a distance x from its mean position. From Newton's second Law,

$$m\ddot{x} + m\gamma\dot{x} = -eE \quad (1.1)$$

Where $-eE$ is the restoring force of the positive ion and $\gamma = \frac{1}{\tau}$ is the characteristic damping frequency. This corresponds to the energy losses that occur due to energy transitions within the conduction band (interband transitions having nearly continuous energies). Assuming x and E both have harmonic dependence, that is $x = x_0 \exp(-i\omega t)$ and $E = E_0 \exp(i\omega t)$,

$$x_0 = \frac{e}{m(\omega^2 + i\gamma\omega)} E \quad (1.2)$$

Polarization $P = -nex$ can be used to calculate the bulk response of the material. Putting this into Eqn. 1.2,

$$P = \frac{-ne^2}{m(\omega^2 + i\gamma\omega)} E \quad (1.3)$$

$$\epsilon(\omega) = 1 - \frac{\omega_p^2}{\omega^2 + i\omega\gamma} \quad (1.4)$$

Where $\omega_p = \sqrt{\frac{ne^2}{\epsilon_0 m}}$ is termed as the plasma frequency of the material. Thus, using the Drude model, a frequency dependent dielectric constant can be obtained from Eqn. 1.4. The real part of ϵ determines the degree of polarization. The complex part of ϵ leads to phase shifts between the incident field and polarization field. The complex refractive index $\tilde{n} = n + i\kappa$ is related to the dielectric constant by $\tilde{n} = \sqrt{\epsilon}$. It can be shown that the absorption coefficient $\alpha(\omega) = \frac{2\kappa(\omega)\omega}{c}$. The absorption in the Drude model corresponds to the intraband transitions. Intraband transitions result in non-equilibrium higher energy electrons also termed as 'hot electrons'. These electrons equilibrate by losing energy thermally leading to the 'thermoplasmonic' effect. However, hot electrons can be strategically extracted using a Schottky junction and used for conduction in a semiconductor. This strategy is used in photodetectors, photocatalysts, photovoltaic cells, etc.

The Drude Model provides a reasonably good approximation for the dielectric function in certain frequency ranges. However, this model completely breaks down in the range of interband transitions, which are also termed as Landau Damping. The main transition relevant to this report is the excitation of electrons from the d-orbital of gold into the s-orbital which occurs in the ultraviolet region. These transitions manifest as an increase in the value of the imaginary part of ϵ .

1.3 Quasistatic Approximation

Now that the dielectric function of the nanoparticle is obtained it can be implemented to obtain results based on appropriate boundary conditions. The most simple geome-

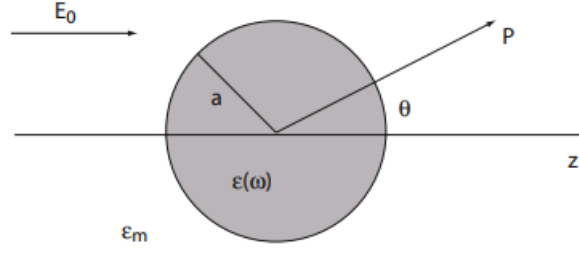


Figure 1.3: Quasistatic Approximation. [18]

try to solve for is a sphere with linearly polarized plane wave incident on it. Consider a sphere with diameter a embedded in a medium with dielectric function ϵ_m . In the case of $a \ll \lambda$, it can be assumed that there is minimal spatial variation in the incident field experienced by the particle. At the resonant frequency the charge density forms a standing wave which can be represented as $\rho(\mathbf{r}) = \rho_0(\mathbf{r}) \exp(-i\omega t)$. Moreover, we can preliminary neglect the temporal effects, by considering the charge density wave at its extremum. These assumptions leads to a problem involving only an uniform electrostatic field ('quasistatic limit'). Consider a uniform field $E_0 \hat{z}$ as shown in Fig. 1.3.

Thus, this electrostatic problem can be solved using the Laplace Equation $\nabla^2 \phi = 0$, from which the electric field can be obtained $\mathbf{E} = -\nabla \phi$. Implementing azimuthal symmetry and solving with appropriate boundary conditions, we obtain

$$\Phi_{\text{in}}(r, \omega) = \frac{3\epsilon_m}{\epsilon(\omega) + 2\epsilon_m} E_0 r \cos \theta \quad (1.5)$$

$$\Phi_{\text{out}}(r, \omega) = -E_r \cos \theta + \frac{\epsilon(\omega) - \epsilon_m}{\epsilon(\omega) + 2\epsilon_m} E_0 a^3 \frac{\cos \theta}{r^2} \quad (1.6)$$

Eqn. 1.6 can be interpreted as the superposition of the external field and a point dipole located at the particle center. Using this, dipole moment and hence polarizability can be defined

$$p = 4\pi\epsilon_0\epsilon_m a^3 \frac{\epsilon(\omega) - \epsilon_m}{\epsilon(\omega) + 2\epsilon_m} E_0 \quad (1.7)$$

$$\alpha = 4\pi a^3 \frac{\epsilon(\omega) - \epsilon_m}{\epsilon(\omega) + 2\epsilon_m} \quad (1.8)$$

Using $\mathbf{E} = -\nabla \Phi$:

$$\mathbf{E}_{\text{in}} = \frac{3\epsilon_m}{\epsilon + 2\epsilon_m} \mathbf{E}_0 \quad (1.9)$$

$$\mathbf{E}_{\text{out}} = \underbrace{\mathbf{E}_0}_{\text{far field}} + \underbrace{\frac{3\mathbf{n}(\mathbf{n} \cdot \mathbf{p}) - \mathbf{p}}{4\pi\epsilon_0\epsilon_m} \frac{1}{r^3}}_{\text{near field}} \quad (1.10)$$

Thus there is a significant amplification of the near field at the resonance frequency. that falls off with r^3 . It is this field amplification that is of interest for applications such as photodetection and SERS.

Resonance occurs when the polarization (or dipole moment) amplitude is the highest, which happens when $|\varepsilon + 2\varepsilon_m|$ reaches a minimum. For low damping limit, this simplifies into the Frölich condition (corresponding to the dipole mode)

$$\text{Re}[\varepsilon(\omega_{\text{LSPR}})] = -2\varepsilon_m \quad (1.11)$$

Higher order resonance modes occur at [24]

$$(l + 1)\varepsilon_m = -l\varepsilon \quad (1.12)$$

Incorporating the time dependence leads to the formation of an oscillating dipole. The electromagnetic fields due to the oscillating dipole can be obtained as follows-

$$\mathbf{H} = \frac{ck^2}{4\pi}(\mathbf{n} \times \mathbf{p}) \frac{e^{ikr}}{r} \left(1 - \frac{1}{ikr}\right) \quad (1.13)$$

$$\mathbf{E} = \frac{1}{4\pi\varepsilon_0\varepsilon_m} \left\{ k^2(\mathbf{n} \times \mathbf{p}) \times \mathbf{n} \frac{e^{ikr}}{r} + [3\mathbf{n}(\mathbf{n} \cdot \mathbf{p}) - \mathbf{p} \left(\frac{1}{r^3} - \frac{ik}{r^2}\right) e^{ikr}] \right\} \quad (1.14)$$

It can be seen that the near field simplifies to the quasistatic limit, making the previous results still valid close to the particle. From Poynting Vector Calculations, the scattered and absorption coefficients can be calculated

$$C_{\text{sca}} = \frac{k^4}{6\pi} |\alpha|^2 = \frac{8\pi}{3} k^4 a^6 \left| \frac{\varepsilon - \varepsilon_m}{\varepsilon + 2\varepsilon_m} \right|^2 \quad (1.15)$$

$$C_{\text{abs}} = k \text{Im}[\alpha] = 4\pi k a^3 \text{Im} \left[\frac{\varepsilon - \varepsilon_m}{\varepsilon + 2\varepsilon_m} \right] \quad (1.16)$$

$$C_{\text{ext}} = 9 \frac{w}{c} \varepsilon_m^{3/2} V \frac{\varepsilon_2}{[\varepsilon_1 + 2\varepsilon_m] + \varepsilon_2^2} \quad (1.17)$$

Where $C_{\text{ext}} = C_{\text{sca}} + C_{\text{abs}}$ is the extinction coefficient. Thus, it can be seen that scattering and absorption both reach their resonant values at the LSPR frequencies. Thus, it has been shown that there is an amplification in the near field, absorption and scattering at the resonant frequencies. Thus, finding the wavelength at which the extinction maxima (apart from interband transitions) occurs gives us the wavelength at which the field amplification will be maximum. It must be noted that the approximation used till now is valid only for nanoparticles below 100nm in visible/NIR regions.

In the applications of interest, it is crucial to know the frequency range in which the field amplification is maximum. Due to the complex nature of ε , there is a broadening of the resonance peak leading to a wider range at which the field amplification is in the useful range. Thus, finding the absorption peaks of a nanostructure by means of spectroscopic techniques can enable us to find the resonant frequency and by implication, the frequency at which the field amplification is maximum. Thus in both simulation spectroscopy experiments, one aims to measure the extinction spectra in order to find the LSPR frequency.

2

Simulations

Various nano-structures were simulated in Ansys Lumerical FDTD to analyse the dependence of their response to light on various properties. These simulations can be used as a predictive tool to help design nanoparticles for a particular application. FDTD (Finite Difference Time Domain) method is powerful numerical analysis technique used for modelling computational electrodynamics. It numerically solves the Maxwell's equations in time domain for a user defined geometry and field excitation. The frequency dependant dielectric constant can be implemented to model the response of a material to an electromagnetic stimulus. Monitors of various types can be placed in the simulation region which enables recording of relevant data. Boundary conditions such as Perfectly Matching Layer, Perfect Conductor, Periodic Boundary Condition, etc are available, and must be chosen appropriately. Just like other Finite Difference Methods, the geometry is meshed, or divided into smaller cells. The accuracy of the simulation can be tuned by varying how fine the mesh is, at the cost of simulation resources. Similarly there is also a discretization of time described by a timestep dt .

The intention of this study is to synthesize helicoidal (Helicoid 432-III) particles having an octahedral geometry as a synthesis intermediate. Thus, apart from the chiral geometry, the response of octahedral particle in the colloid state is of importance. In order to validate the simulation setup being used, the simulation is first run for spheres, for which the analytical solution is known. This analytical solution is built into a script function `mie3d`, which generates the scattering and absorption of a nanoparticle as a function of wavelength, for a given radius and background refractive index. After validating the setup, parameters were varied to assert the results derived in the previous section. After this simulations were carried out for nano-octahedra. Parameters were varied to determine the dependance of the LSPR wavelength. After this, simulations were carried out for the chiral structure in order to determine its circular dichroism.

Important Terminology

1. **Cross Section (σ)** is a measure of the likelihood of a radiative process. It is equal to the power transferred in the radiative process divided by the source intensity.

$$\sigma_i = \frac{P_i}{I_{\text{source}}} \quad (2.1)$$

2. **Mie Efficiency** of an extinction process (absorption or scattering) is defined as

the cross section divided by the projected area of the particle.

$$Q_{i,\text{sphere}} = \frac{\sigma_i}{\pi r^2} \quad (2.2)$$

$$Q_{i,\text{octahedron}} = \frac{\sigma_i}{a^2} \quad (2.3)$$

where a is the edge length of the octahedron.

3. **Circular Dichroism** refers to the differential absorption of right-handed and left-handed circular polarized light. In the simulations carried out, Absorption values are taken to be source normalized.

$$\Delta A = A_L - A_R \quad (2.4)$$

For this study, the only material of interest is gold, hence all other materials are assumed to have a real, frequency invariant dielectric constant. For gold, the dielectric constants obtained experimentally by Johnson and Christy [12] are used. Lumerical fits a polynomial curve onto the given datapoints as seen in Fig. 2.1. The high values of the imaginary refractive index at higher frequencies correspond to the interband transition of d-electrons in gold. Unless mentioned otherwise, the refractive index in the simulations is taken to be equal to 1. Similarly, by default the particle size is taken to be 50nm. Sources inject EM wave in the -ve z direction.

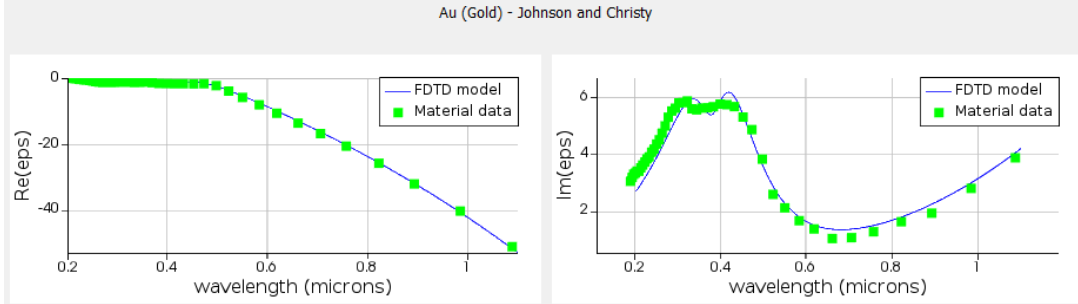


Figure 2.1: Dielectric constant data used for simulations

2.1 Spherical Nanoparticles

For modeling the sphere, the simulation was set up as shown in 2.2. A Total Field Scattering Field (TFSF) source is used which injects an EM wave at one end of a cuboid and annihilates it at the other. Thus there is no effect of the source field outside the cuboidal region. This makes it possible to separate the the field due to the source and the scattered field due to the nanoparticle. Hence cross section analysis groups are placed both inside and outside the source region, to measure the absorption and scattering cross sections separately. The absorption group effectively measures the loss in power within a region, while the scattering group does the opposite and measures the field generated inside its volume. Both analysis groups store the cross section data as a function of the wavelength. Finer meshing was imposed near the particle to reduce the influence of staircasing effect.

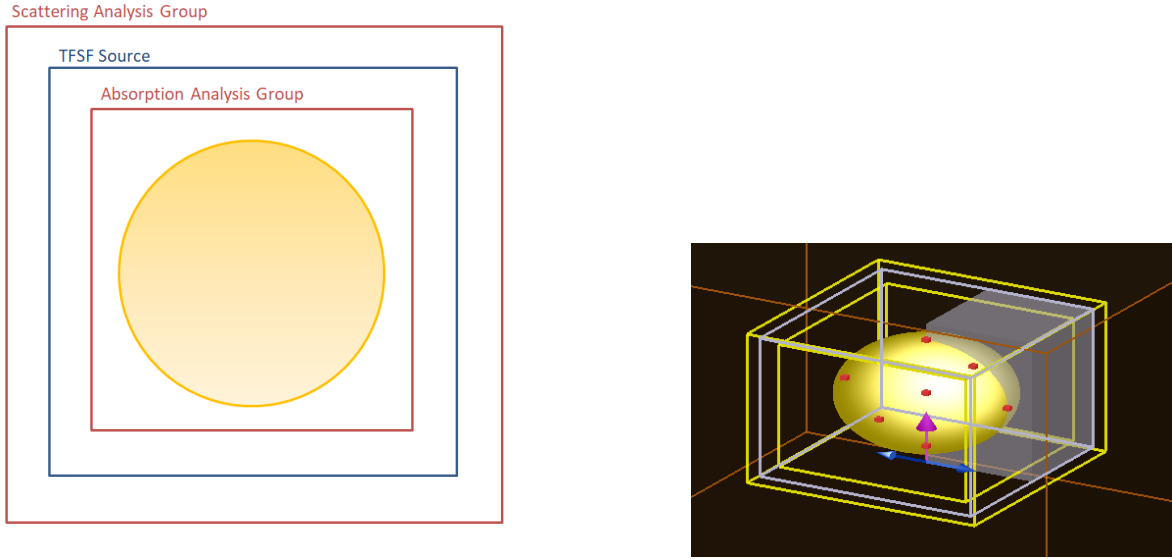


Figure 2.2: *Schematic of simulation setup and perspective view of setup in Lumerical*

Hence, the simulations of a spherical nanoparticle were set up, and the absorption and scattering coefficients were compared to the mie3d data. Based on this, the simulation parameters were optimised until data obtained from the simulation closely matched the expected data. Once the setup was validated for a range of sphere sizes, the geometries of the nanoparticles were varied to obtain their optical responses. These parameter sweeps help obtain insights into designing nanoparticles for a particular end application.

2.1.1 Varying Size

Figures 2.15 show the deviation in Absorption and extinction coefficients from Mie3d for a range of diameters. As mentioned in Eqns. 1.16, 1.15, the absorption scales with volume while scattering scales with V^2 . This can be seen in the same figure that the contribution of scattering to the overall extinction is initially negligible, but increases with size. These simulations have been carried out with background refractive index = 1. A comparison of absorption and scattering is shown in 2.3

2.1.2 Varying Refractive Index

As shown in Eqn 1.11 the LSPR peak undergoes a red-shift with increasing wavelength. This trend is followed in Fig. 2.4

2.2 Octahedral Nanoparticles

The next geometry considered in this section is octahedrons. Since synthesising the final chiral structure involves octahedrons as an intermediate, it is helpful to understand the optical response of the octahedral geometry. Unlike spheres, the LSPR of octahedrons depends on the angle of incidence of the incoming EM wave due to its

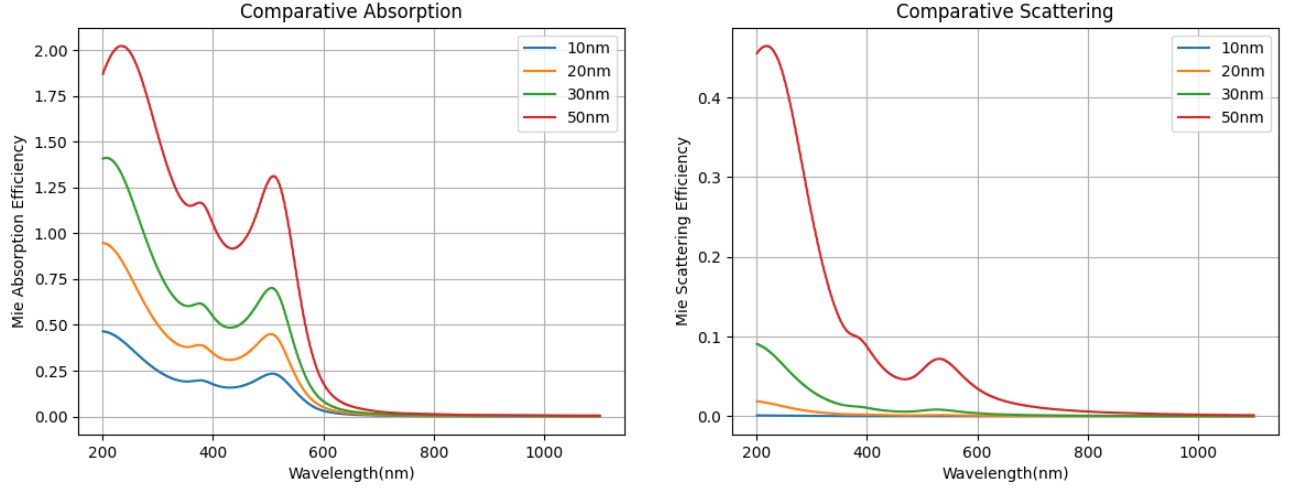


Figure 2.3: *Variation of Absorption and Scattering with sphere diameter*

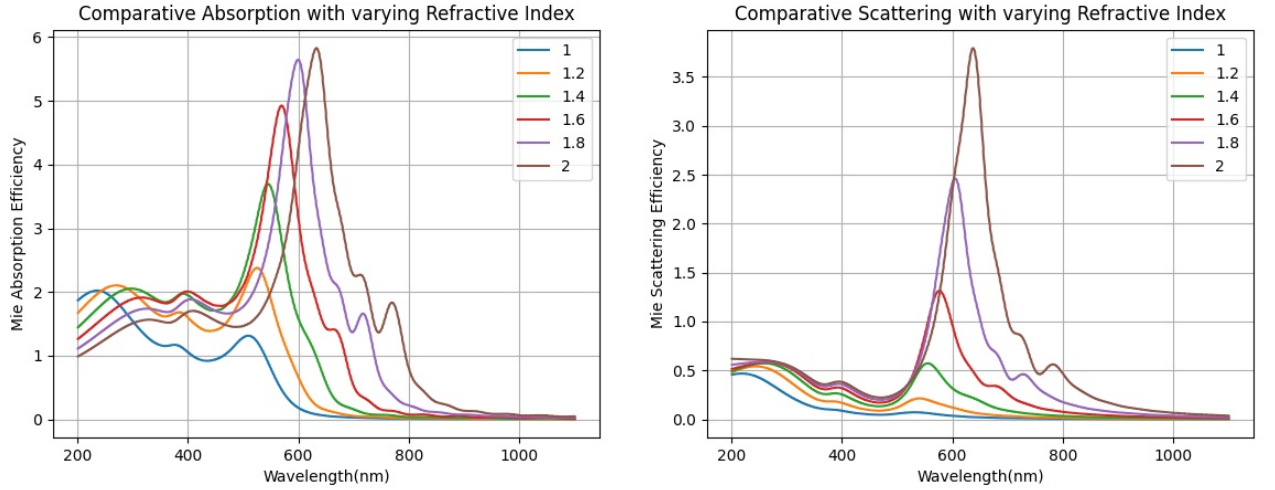


Figure 2.4: *Variation of Absorption and Scattering with refractive index*

geometrical anisotropy Thus, the optical response is an average of all possible orientations in a colloid. Hence this section aims to conduct a Monte-Carlo simulation in which the inclination of the octahedra with respect to the coordinate axes are swept in order to encompass all orientations. Before that, the variation of Absorbance and scattering with size, orientation, and near-field distribution are simulated.

2.2.1 Varying Size

There are two distinct modes at lower sizes which merge into each other as the width of the peaks increase with increasing size. In this simulation the incident wave is propagating along the line connecting two opposite vertices. The size parameter mentioned in the plots and table is the distance between the opposite vertices which is equal to $2a$. Mie efficiency is described in Eqn. 2.3. These simulations are carried out

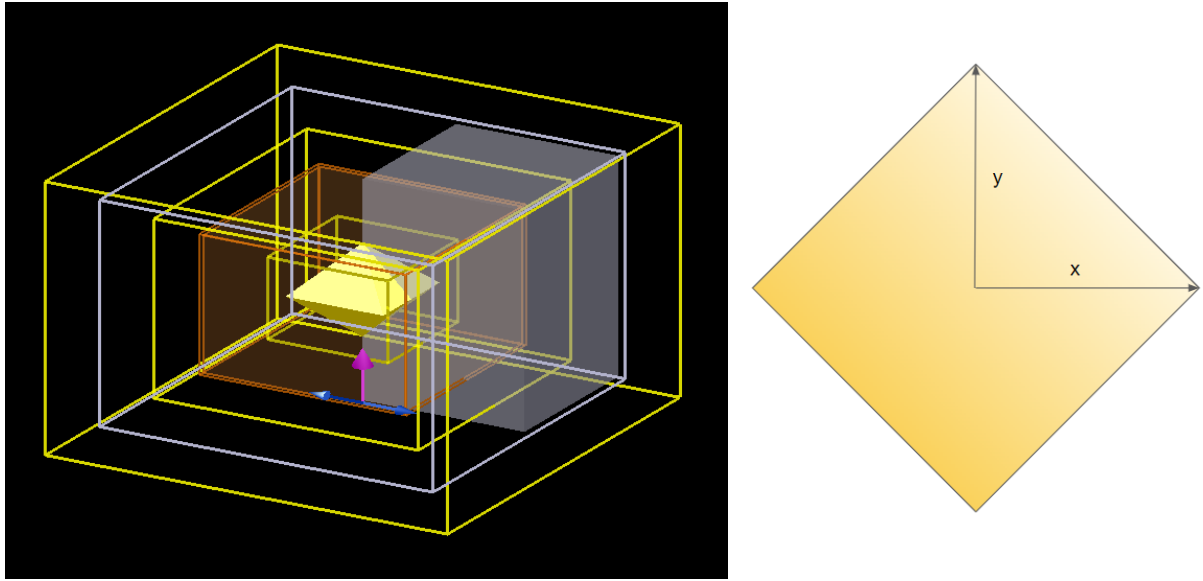


Figure 2.5: *Simulation setup and definition of coordinate system (wave propagation is into the plane)*

with background refractive index = 1.

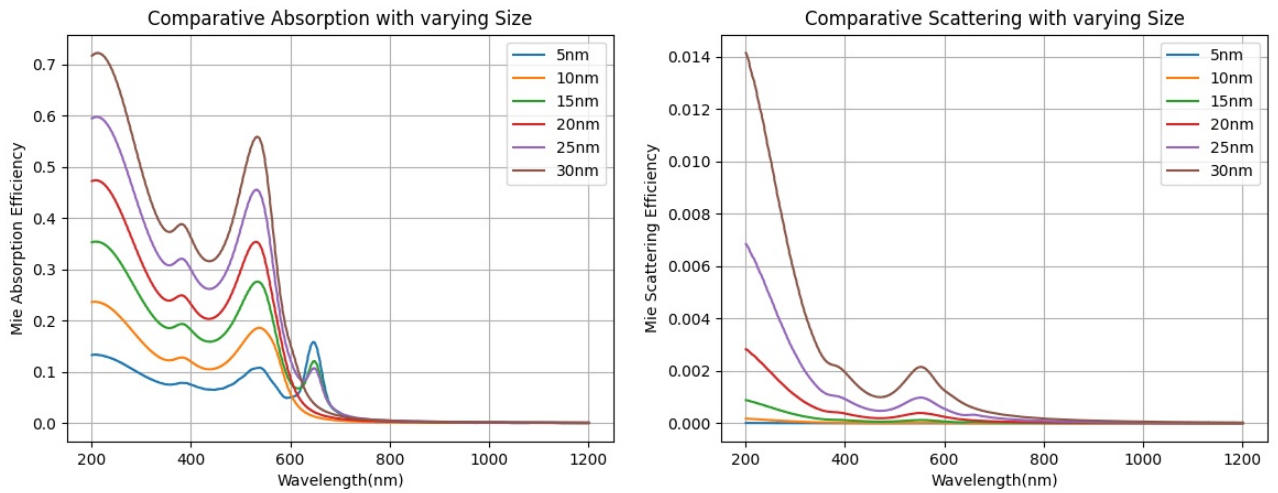


Figure 2.6: *Variation of Absorption and Scattering with octahedron size*

2.2.2 Varying Orientation

The inclination of the octahedra with respect to the propagation direction (z) as well as the polarization direction (x) is shown. As expected, there is a variation in the position and shape of the LSPR peak.

2.2.3 Field Enhancement

The spatial electric field distribution as a function of wavelength is calculated using a 3D DFT field monitor. The field intensification is shown for an arbitrary wavelength

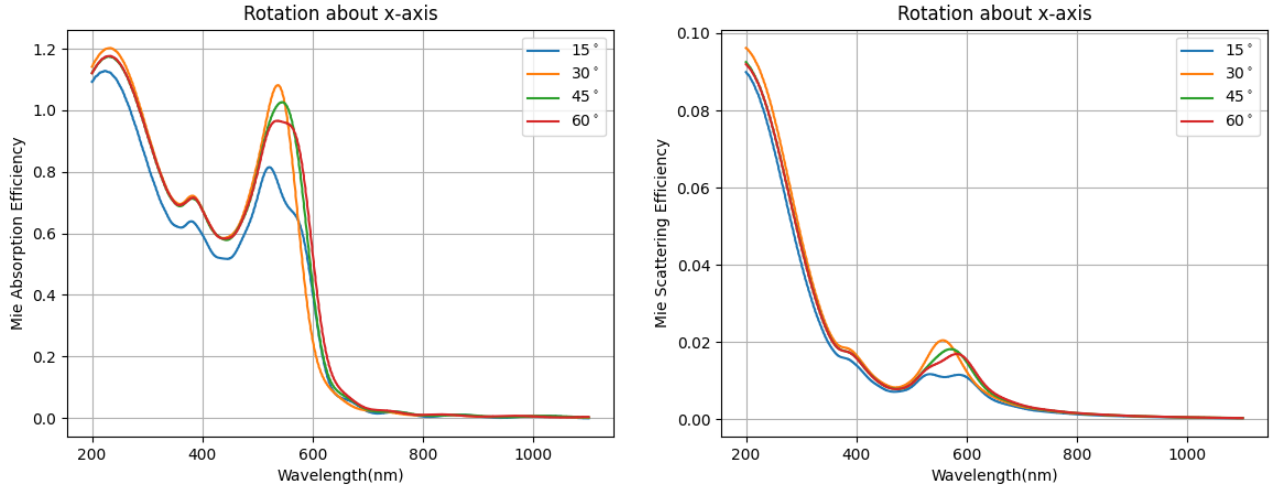


Figure 2.7: Variation of Absorption and Scattering with octahedron inclination to defined x-axis

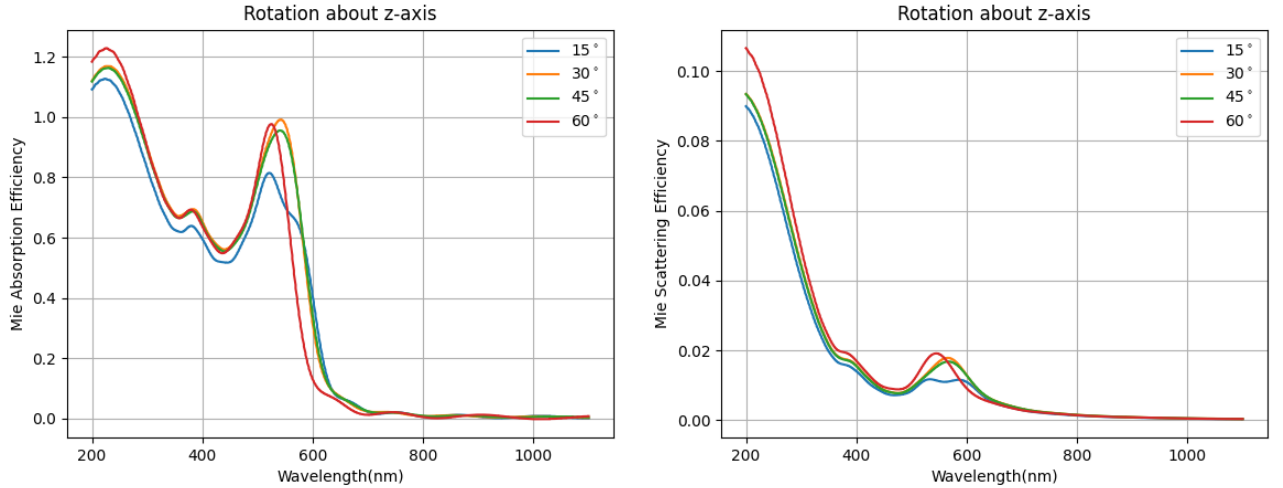


Figure 2.8: Variation of Absorption and Scattering with octahedron inclination to defined z-axis

(300nm) and the LSPR wavelength (561nm). As shown in Fig 2.9, the maximum intensification factor is 16.4. This occurs in sharp regions (or 'hotspots').

2.2.4 Monte-Carlo Simulation

In order to obtain the average response of a randomly oriented array of octahedrons, such as would be expected in a colloid, Monte Carlo simulations were carried out by varying the orientation angles. The average of all the simulations is exhibited in Fig. 2.11. The angles were assumed to have a uniform probability distribution and coupling effects were neglected. 50 simulation runs were carried out (2.10) in order to obtain a sufficiently unbiased set. Thus it can be seen that there is a major peak broadening that takes place which is similar to the UV-Vis spectra seen in various literature. Once the refractive index of the solvent has been obtained, it can be used to

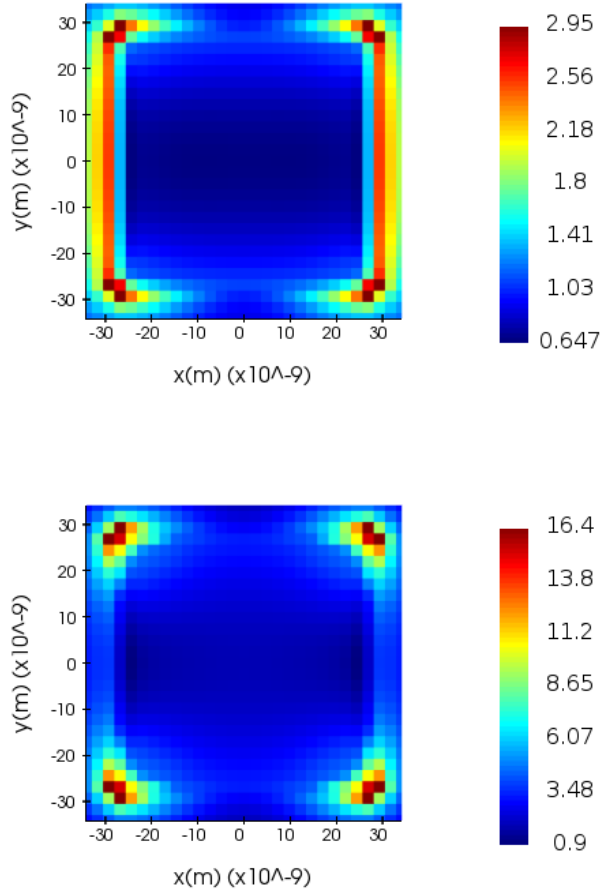


Figure 2.9: *Plasmonic field intensification of octahedron nanoparticles at the midplane perpendicular to the direction of propagation corresponding to wavelengths 300nm (top) and 561nm (bottom)*

obtain an estimate on the size of the nanoparticles in a colloid without the requirement of microscopy.

2.3 Helicoidal Particles

The Helicoid 432 III geometry was generated using SolidWorks and imported into Lumerical. As shown in Fig. 3.2, this geometry has 4-fold, 3-fold and 2-fold rotation axes. The refractive index profile of the nanoparticles was measured by a monitor to ensure that there was no error in the imported geometry. The performance parameter for chiral particles is not the extinction spectra, but the preferential absorption, or circular dichroism. In this section the model simulated is the chiral nanoparticles of size 60nm dispersed in a periodic array having period 120nm on a dielectric substrate with refractive index 1.4 as shown in Fig. 2.12. The periodic array is simulated by modeling a single particle and applying a periodic boundary condition in the x- and y- extremities.

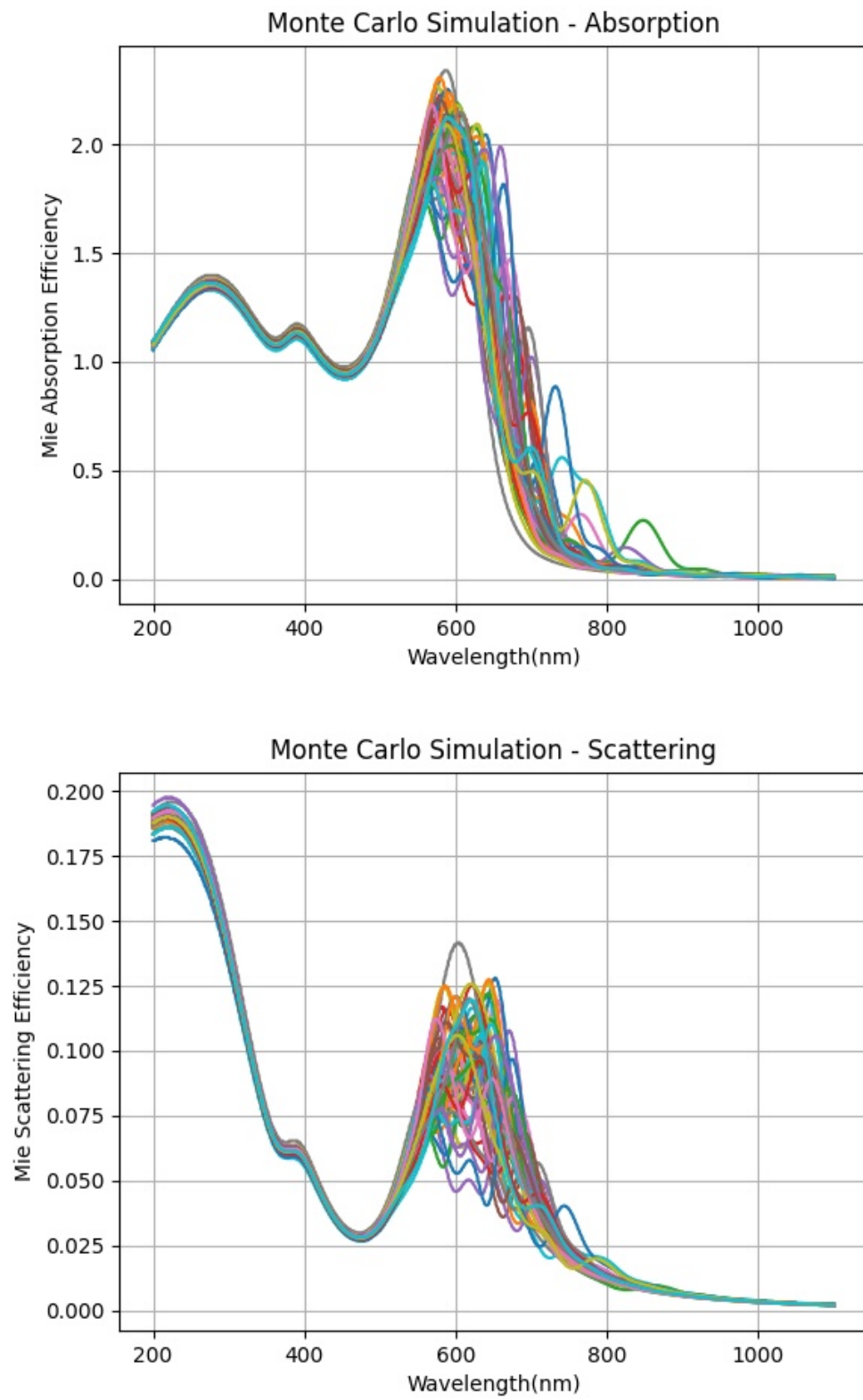


Figure 2.10: Monte-Carlo Simulations corresponding to varying orientation

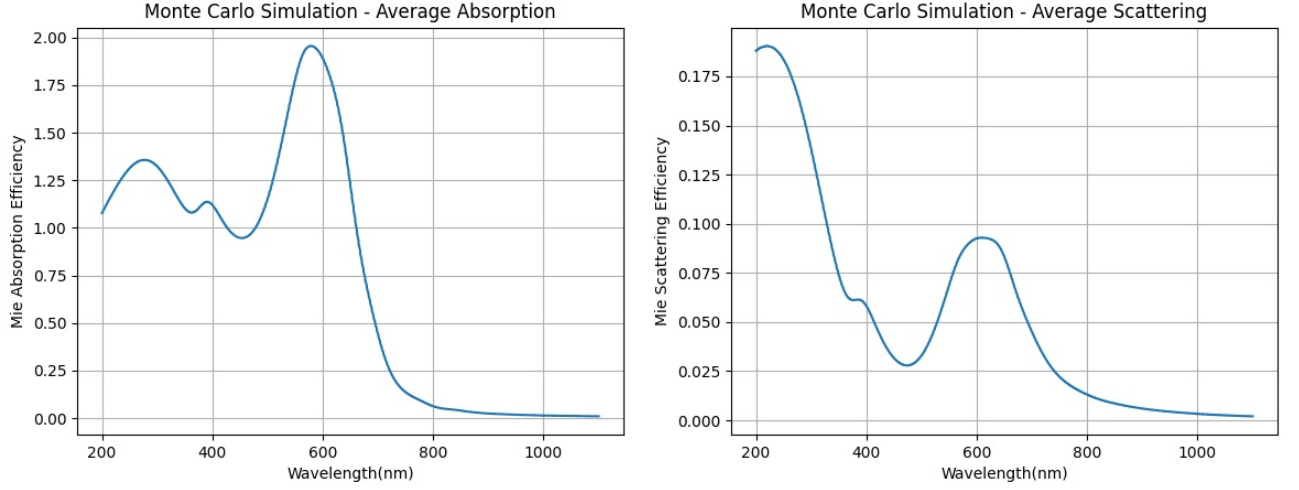


Figure 2.11: Average absorption and scattering results from Monte Carlo Simulations

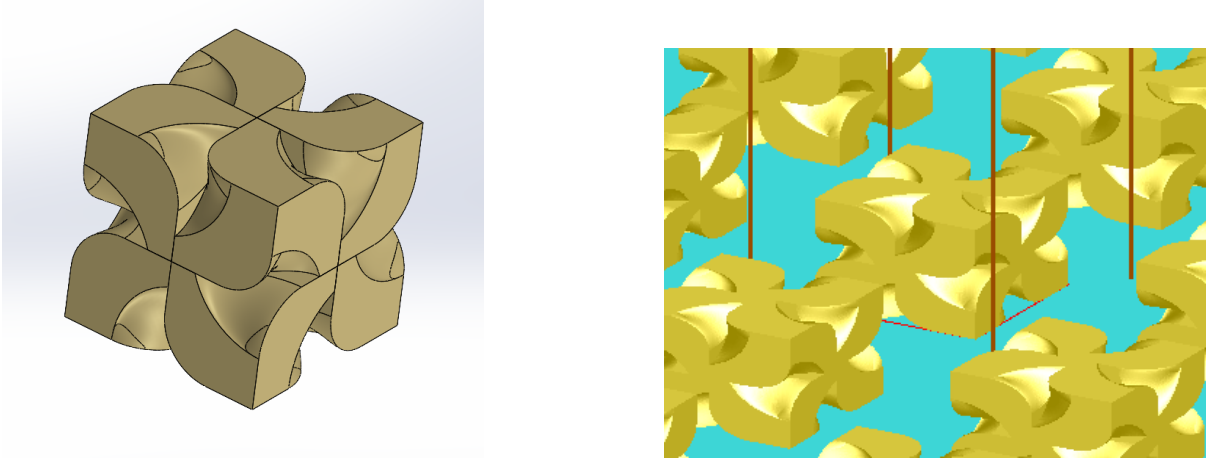


Figure 2.12: CAD of Helicoid created in SolidWorks (left) and setup of geometry in Lumerical (right)

2.3.1 Circular Polarized Light

The most straightforward way to generate circular polarized light in a simulation is to use two linearly polarized sources perpendicular to each other and with a phase difference of 90° . However, this requires two simulations to be run, corresponding to left and right circular polarizations. However, by exploiting the inherent 4-fold symmetry present along the transmission axis, one linearized polarized source is sufficient to test the circular dichroism performance, that too in only one simulation run.

Consider $E_x(x, y, z)$ and $E_y(x, y, z)$ to be the electric field distributions corresponding to x - and y - polarized light respectively. Then, the fields corresponding to right hand polarization and left hand polarization are given by:

$$E_R(x, y, z) = E_x(x, y, z) + E_y(x, y, z) \exp(i\frac{\pi}{2}) \quad (2.5)$$

$$E_L(x, y, z) = E_x(x, y, z) + E_y(x, y, z) \exp(-i\frac{\pi}{2}) \quad (2.6)$$

Let x, y, z superscripts correspond the component field in the denoted direction. Due

to the four-fold symmetry, the y-polarized field distribution can be obtained from the x-polarized field distribution by a co-ordinate transformation (rotating axes by 90°). Thus,

$$\begin{bmatrix} E_y^x \\ E_y^y \\ E_y^z \end{bmatrix} = \begin{bmatrix} \cos(\frac{\pi}{2}) & -\sin(\frac{\pi}{2}) & 0 \\ \sin(\frac{\pi}{2}) & \cos(\frac{\pi}{2}) & 0 \\ 0 & 0 & 1 \end{bmatrix} \begin{bmatrix} E_x^{x'} \\ E_x^{y'} \\ E_x^{z'} \end{bmatrix} \quad (2.7)$$

$$E_y^x(x, y, z) = -E_x^y(y, -x, z) \quad (2.8)$$

$$E_y^y(x, y, z) = E_x^y(y, -x, z) \quad (2.9)$$

$$E_y^z(x, y, z) = E_x^z(y, -x, z) \quad (2.10)$$

Substituting into Eqns. 2.5 and 2.6,

$$E_R^x(x, y, z) = E_x^x(x, y, z) - E_x^y(y, -x, z) \exp(i\frac{\pi}{2}) \quad (2.11)$$

$$E_R^y(x, y, z) = E_x^y(x, y, z) + E_x^y(y, -x, z) \exp(i\frac{\pi}{2}) \quad (2.12)$$

$$E_R^z(x, y, z) = E_x^z(x, y, z)(1 + \exp(i\frac{\pi}{2})) \quad (2.13)$$

and

$$E_L^x(x, y, z) = E_x^x(x, y, z) - E_x^y(y, -x, z) \exp(-i\frac{\pi}{2}) \quad (2.14)$$

$$E_L^y(x, y, z) = E_x^y(x, y, z) + E_x^y(y, -x, z) \exp(-i\frac{\pi}{2}) \quad (2.15)$$

$$E_L^z(x, y, z) = E_x^z(x, y, z)(1 + \exp(-i\frac{\pi}{2})) \quad (2.16)$$

Thus, knowing the field distribution due to one linearly polarized source can be used to obtain the circular-dichroism spectra of a structure. These equations are implemented into the Lumerical script, and field data from the monitors is manipulated accordingly. Poynting vector calculations are then used to find the power transmitted through a certain monitor.

2.3.2 Circular Dichroism

Circular dichroism for the setup is shown in 2.13.

2.3.3 Field Enhancement

Field enhancement profile for the face of the particle is shown in 2.14. The maximum field intensification of 28.2 is seen in this particle's hotspot at its LSPR wavelength of 627nm.

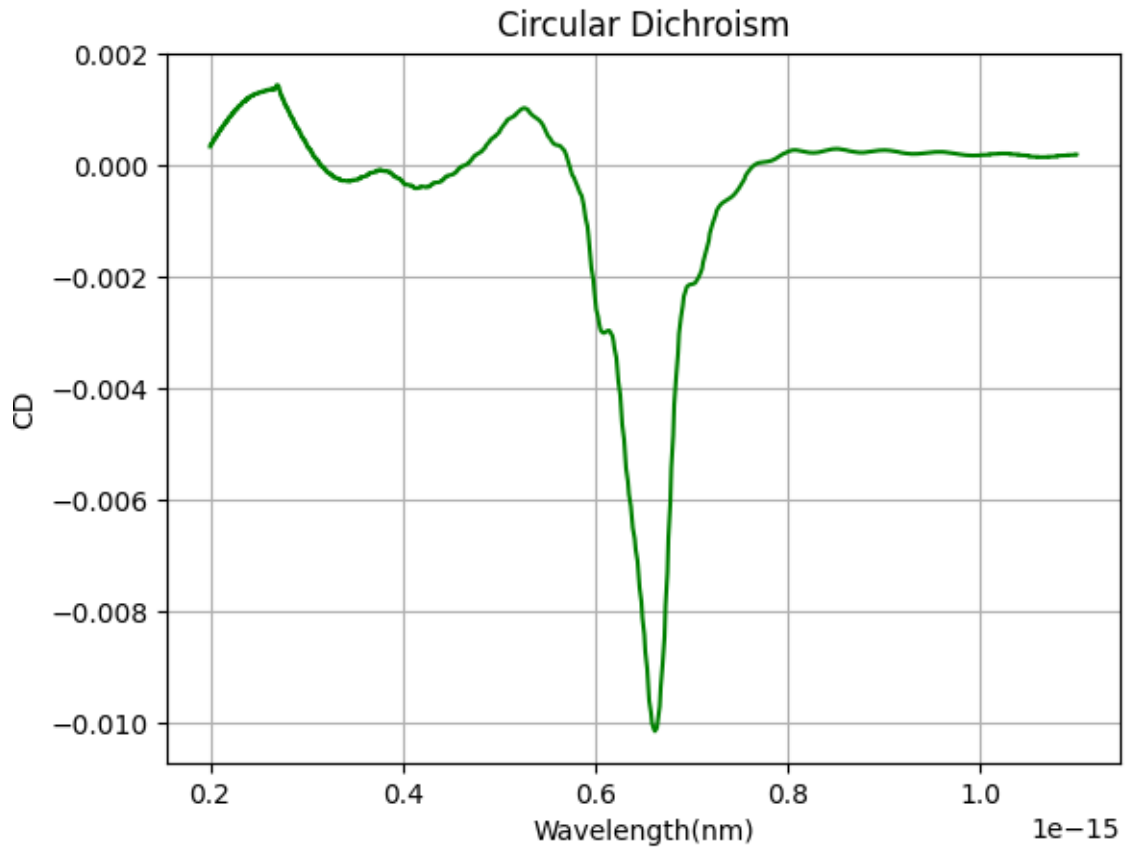


Figure 2.13: Circular Dichroism simulation of helicoidal nanoparticle in periodic array

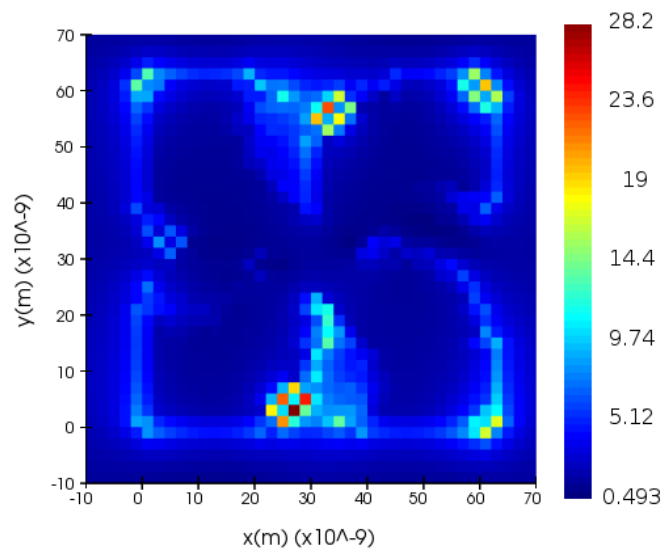
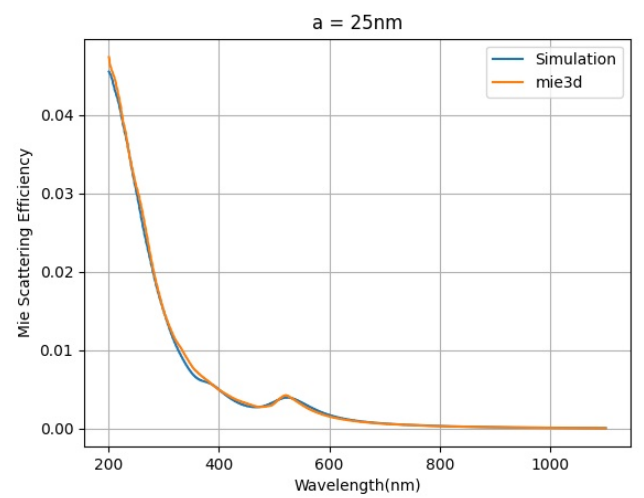
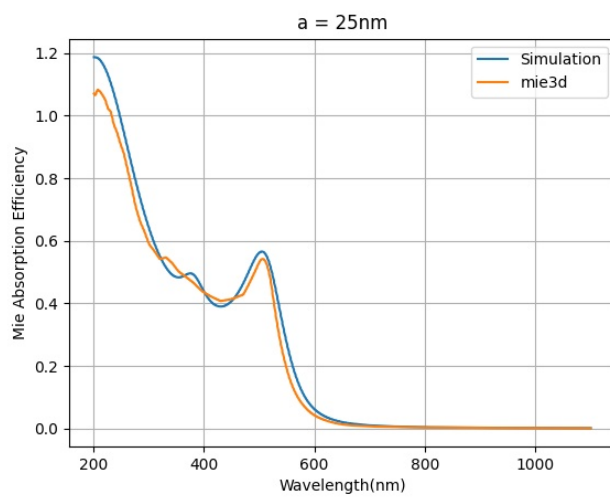
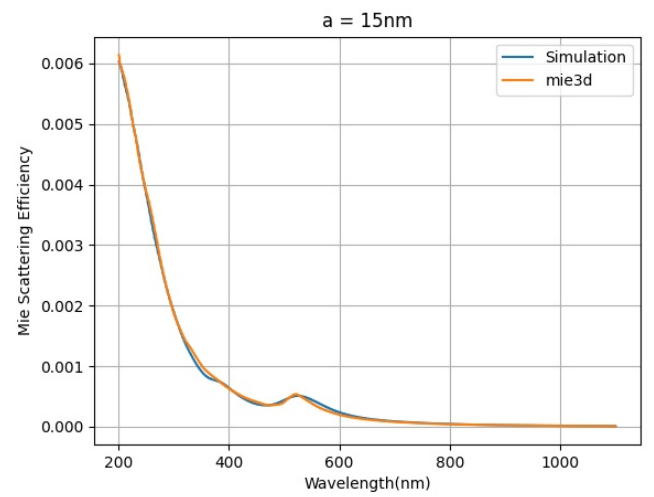
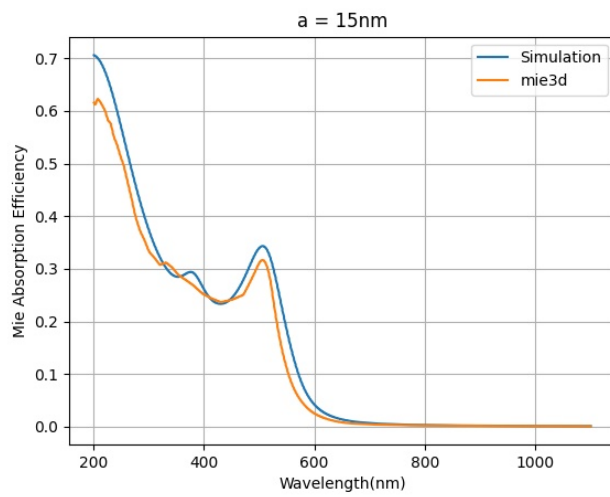
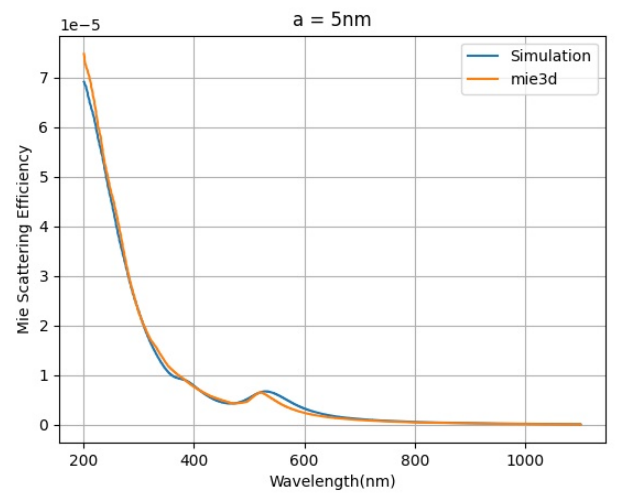
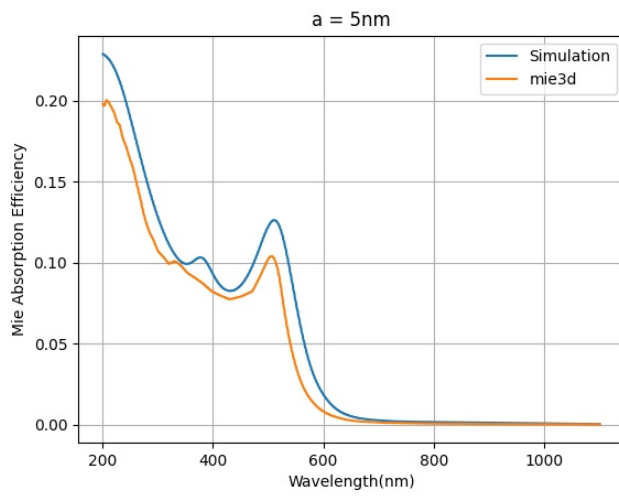


Figure 2.14: Plasmonic field intensification at face of helicoid perpendicular to incident light at 627nm



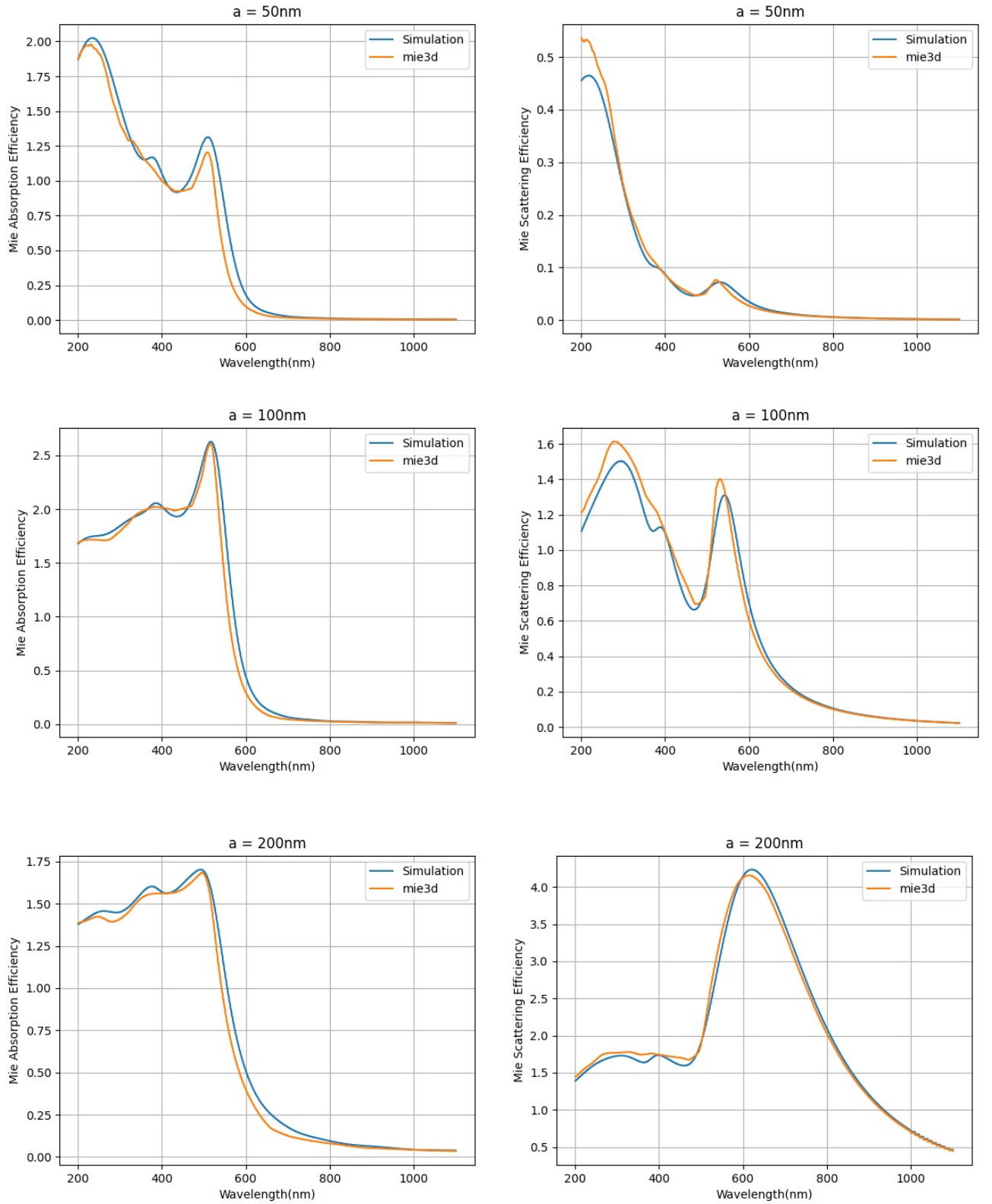


Figure 2.15: Variation of Mie Absorption Efficiency (left) and Mie Scattering (right) with change in particles size. The simulated data is compared with built in function `mie3d` for comparison.

3

Synthesis

There are various approaches to achieve shape control of nanoparticles which can be divided into "bottom-up" and "top-down" pathways. The "top-down" approaches involve generating the nanostructures from a large material entity using physical and lithographic principles. Inversely, in "bottom-up" approaches, the particles are grown or assembled from their atomic, ionic or molecular units. These synthesis routes offer much more control over the morphology, composition and size of the nanoparticles. Examples of such methods are precipitation, seed-mediated approach, polyol approach, template approach, electrochemical synthesis and photochemical synthesis [33]. This report focuses on the seed mediated synthesis of gold nanoparticles, which is a solution state bottom-up method. An efficient synthesis methodology for chiral particles mentioned in previous literature [21][15][14][13][5] is taken as a reference, after which various parameters will be optimized to achieve optimal results. It involves synthesis of gold nano-octahedra as an intermediate after which the nanoparticles are further grown into the final chiral morphology Helicoid 432. This section contains a review of the seed mediated process, followed by the experimental parameters used by us while synthesizing gold nano-octahedra.

3.1 Literature Review

3.1.1 Seed Mediated Synthesis

Seed Mediated synthesis has been used to obtain a wide variety of morphologies including simple polyhedra, plates as well as exotic structures with high index facets and concave surfaces. It involves reduction of a metal salt into small nuclei (or seeds) after which a controlled growth is carried out [25]. It is carried out in two major steps:

1. Rapid reduction to form small, highly monodisperse spherical 'seeds', which serve as nucleation sites
2. Controlled Reduction of Au onto seeds to achieve desired shape and size

The separation of the nucleation and growth phases ensures particles with uniformity in their properties.

Nucleation Step

The first step is largely the same in most literature -reduction of HAuCl_4 (Au^{3+} ions) with a strong reducing agent like NaBH_4 in the presence of a stabilizer. These include sodium citrate, as well as surfactants such as CTAC and CTAB (cetyl triammonium chloride/bromide), which prevent the dispersed phase from agglomerating. A strong reducing agent is chosen to ensure that nucleation is rapid enough, which ensures growth does not take place. The seed solution thus created has monodisperse single crystal particles generally having a size of 3-7nm.

Growth Step

The second step, or the growth phase involves controlling the reaction parameters in order to stabilize specific crystallographic planes, which decides the nanoparticle morphology. Examples of such geometries include {111} faceted octahedra, {100} faceted cubes, {110} faceted bipyramids and {210} faceted hexagonal bipyramids. This shape control can be achieved due to the fact that different crystallographic planes have different surface energies corresponding to their 'dangling bonds'. In this step, a weak reducing agent (Ascorbic Acid) is added to a solution of stabilized Au^{3+} ions after which the seed is introduced. The seeds provide sites for nucleation, which implies that increasing the number of seeds will increase the number of particles, albeit with a smaller size. The concentration of Au^{3+} decides the extent to which the particles can grow, determining their size.

At lower pH values Ascorbic Acid is only able to reduce Au^{3+} to Au^+ , which prevents the formation of fresh nuclei. These Au^+ ions attach to the seed surfaces, which catalyzes their reduction to Au, thus resulting in growth. The nature of the growth is kinetically controlled, that is, effectively controlled by the rate of formation of Au^+ which ultimately depends on the concentration of Ascorbic Acid. At higher Ascorbic Acid concentrations, a kinetically favoured product with high energy facets is formed. On the other hand, at low concentrations, a low energy faceted thermodynamically favoured product obtained.

Apart from the concentration of Ascorbic Acid, the kinetics of the reaction can also be modulated by the addition of halide ions. These ions form monodentate complexes with the Au^+ ions which influence the growth rate of the nanoparticles. The reduction potential of the Au-Halide complexes are in the following order $[\text{AuCl}] < [\text{AuBr}] < [\text{AuI}]$, meaning that $[\text{AuCl}]$ (the complex that exists in the solution in the absence of externally added halide ions) is the most easily reduced. This is due to the fact that solubilities of the complexes decrease with increasing size of the halide ion. Thus for the same concentration parameters, there is a decrease in the equilibrium concentration of solvated Au^+ ions. Addition of larger halide ions results in a decrease in the rate of the reaction, leading to structures having more stable facets.

The growth step can be subdivided into multiple growth 'sub-stages' to achieve a more accurate control over the reaction progress. The effect of varying the concentration of one reagent while keeping other parameters constant is summarized below in Table 3.1

Reagent	Effect of increasing concentration
Seed	Larger number of particles with a smaller size
Au^{3+}	Larger Particles
Ascorbic Acid	Favours higher energy facets
Halide ion	Larger halide ions favour lower energy facets

Table 3.1: *Impact of varying concentrations of reagents*

3.1.2 Chirality

Chirality can be imparted into a nanoparticle by involving an enantiomeric reagents such as L-cysteine and L-Glutathione. This is due to the fact that there is an intrinsic chirality of certain crystallographic planes that rises up from the nature of stacking of crystallographic planes. Higher index planes are a combination of terraces of lower index planes, which imparts a handedness to them. Thus these chiral planes form pairs of non superimposable mirror images. For example, (643) planes can not be superimposed on their corresponding mirror image plane $(\bar{6}4\bar{3})$. This is depicted in Fig. 3.1. From this figure, the origin of the chirality can be seen in the terraces. Chiral facets must be high index Miller planes with $h \neq k \neq l$ and $h \times k \times l \neq 0$. [28]

When an achiral plane, for example, (520) is evolving into a chiral plane (521) , there is an equal preference to the formation of both enantiomeric products. However, in the presence of a chiral reagent, one enantiomeric plane is promoted leading to a chiral structure. This is because the chiral reagent binds preferentially to one enantiomer, thereby stabilizing it and suppressing its growth [21]. This leads to the breakdown of mirror symmetry in the nanoparticles as shown in Fig. 3.2. Thus, involving a specific chiral reagent in the growth stage can be used to direct the growth into a chiral structure.

Based on this information, an intuition regarding shape control of gold nanoparticles can be gained. This can be used to create nanoparticles with specific geometries and sizes fulfilling the requirements of a particular application.

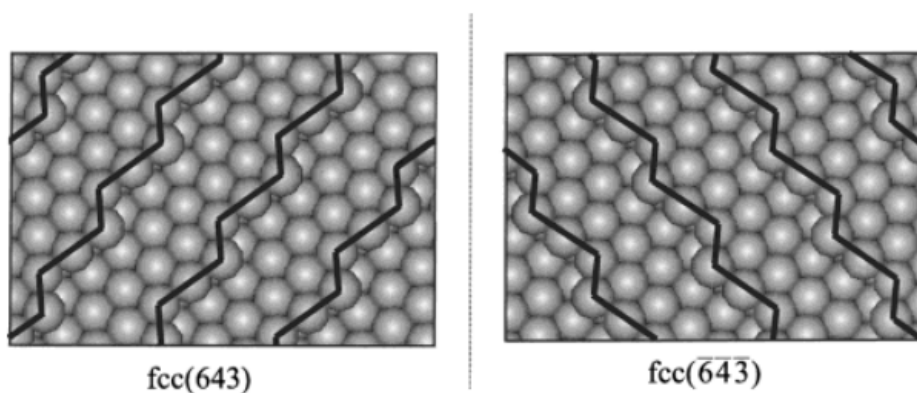


Figure 3.1: *Ball models of FCC (643) and $(\bar{6}4\bar{3})$ surfaces with step edges highlighted. The dotted line represents a mirror plane. [28]*

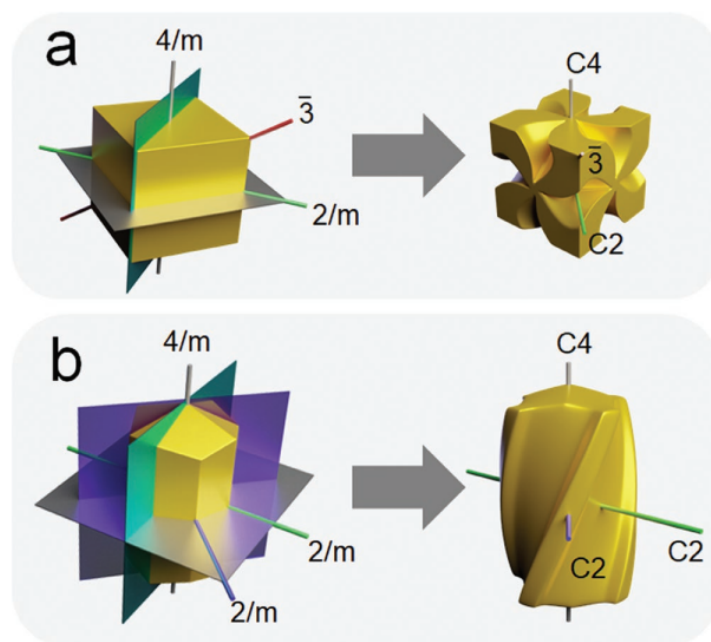


Figure 3.2: Evolution of space groups with mirror symmetries into chiral space groups [21]

3.2 Experimental Work

3.2.1 Octahedral Nanoparticles

As mentioned in the earlier section, octahedra are an intermediate in the synthesis of helicoids. Hence the preliminary step is to synthesize gold nano-octahedra. I have done this following the pathway described in previous literature [31]. It uses HAuCl_4 as a source of gold cations, ascorbic acid as the weak reducing agent and CTAC as the surfactant. I^- ions are also added to slow down the reaction and favour the formation of the thermodynamically favoured product. This method carries out the growth phase in two separate substeps, denoted as step A and B.

Synthesis Steps

Seed particles are prepared by adding 0.25 mL of 0.01M HAuCl_4 , 5mL of 0.2M CTAC and 0.45mL of 0.02M NaBH_4 and diluting with water to 10mL, which is then aged in 30°C water. Solution turns brown as shown in Fig. 3.3. Two identical growth solutions (A and B) are prepared containing 25mM HAuCl_4 , 0.1M CTAC and 0.05mM KI. The concentration of Ascorbic Acid is varied to control the kinetics of the reaction. To growth solution A $55\mu\text{L}$ of seed solution is added leading to the solution turning red. $55\mu\text{L}$ of this growth solution is added to solution B, which turns light pink. This experiment was designed such that growth solution B contains gold octahedrons.

3.2.2 Future Work

The next step in the process is iterative characterization and synthesis to obtain sufficiently accurate octahedrons having only $\{111\}$ planes, which is imperative for the synthesis of helicoids by the pathway mentioned [5]. Characterization is to be car-

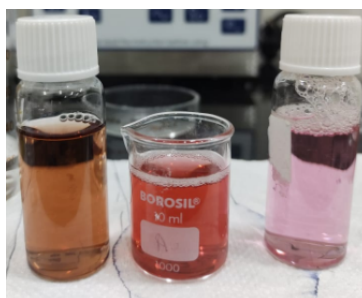


Figure 3.3: (left to right) *Seed Solution, Growth Solution A, Growth Solution B as synthesized*

ried out using UV-Vis spectroscopy and SEM. Helicoid synthesis using L-Glutathione will be initiated after that. Using data from simulations and understanding of growth mechanisms, attempts will be made to tune synthesis parameters to optimize the circular dichroism.

Bibliography

- [1] Hyo-Yong Ahn, Hye-Eun Lee, Kyoungsuk Jin, and Ki Tae Nam. Extended gold nano-morphology diagram: synthesis of rhombic dodecahedra using ctab and ascorbic acid. *Journal of Materials Chemistry C*, 1(41):6861–6868, 2013.
- [2] Nathan D Burrows, Samantha Harvey, Fred A Idesis, and Catherine J Murphy. Understanding the seed-mediated growth of gold nanorods through a fractional factorial design of experiments. *Langmuir*, 33(8):1891–1907, 2017.
- [3] Nathan D Burrows, Wayne Lin, Joshua G Hinman, Jordan M Dennison, Ariane M Vartanian, Nardine S Abadeer, Elissa M Grzincic, Lisa M Jacob, Ji Li, and Catherine J Murphy. Surface chemistry of gold nanorods. *Langmuir*, 32(39):9905–9921, 2016.
- [4] Jie Cao, Tong Sun, and Kenneth TV Grattan. Gold nanorod-based localized surface plasmon resonance biosensors: A review. *Sensors and actuators B: Chemical*, 195:332–351, 2014.
- [5] Nam Heon Cho, Gi Hyun Byun, Yae-Chan Lim, Sang Won Im, Hyeohn Kim, Hye-Eun Lee, Hyo-Yong Ahn, and Ki Tae Nam. Uniform chiral gap synthesis for high dissymmetry factor in single plasmonic gold nanoparticle. *ACS nano*, 14(3):3595–3602, 2020.
- [6] Miharū Eguchi, Daisuke Mitsui, Hsin-Lun Wu, Ryota Sato, and Toshiharu Teranishi. Simple reductant concentration-dependent shape control of polyhedral gold nanoparticles and their plasmonic properties. *Langmuir*, 28(24):9021–9026, 2012.
- [7] Eric SA Goerlitzer, Aniket S Puri, Jebin J Moses, Lisa V Poulikakos, and Nicolas Vogel. The beginner’s guide to chiral plasmonics: Mostly harmless theory and the design of large-area substrates. *Advanced Optical Materials*, 9(16):2100378, 2021.
- [8] Herman Gudjonson, Mikhail A Kats, Kun Liu, Zhihong Nie, Eugenia Kumacheva, and Federico Capasso. Accounting for inhomogeneous broadening in nano-optics by electromagnetic modeling based on monte carlo methods. *Proceedings of the National Academy of Sciences*, 111(6):E639–E644, 2014.
- [9] David Holec, Phillip Dumitraschkewitz, Dieter Vollath, and Franz Dieter Fischer. Surface energy of au nanoparticles depending on their size and shape. *Nanomaterials*, 10(3):484, 2020.
- [10] Sang Hyuk Im, O Ok Park, Yong Taik Lim, et al. Evolution of gold nanoparticles through catalan, archimedean, and platonic solids. *CrystEngComm*, 12(1):116–121, 2010.

- [11] Julie A Jenkins, Terianna J Wax, and Jing Zhao. Seed-mediated synthesis of gold nanoparticles of controlled sizes to demonstrate the impact of size on optical properties. *Journal of Chemical Education*, 94(8):1090–1093, 2017.
- [12] Peter B Johnson and R-WJPrB Christy. Optical constants of the noble metals. *Physical review B*, 6(12):4370, 1972.
- [13] Jeong Won Kim, Nam Heon Cho, Yae-Chan Lim, Sang Won Im, Jeong Hyun Han, and Ki Tae Nam. Controlling the size and circular dichroism of chiral gold helioids. *Materials Advances*, 2(21):6988–6995, 2021.
- [14] Sejeong Kim, Yae-Chan Lim, Ryeong Myeong Kim, Johannes E Fröch, Thinh N Tran, Ki Tae Nam, and Igor Aharonovich. A single chiral nanoparticle induced valley polarization enhancement. *Small*, 16(37):2003005, 2020.
- [15] Yoon Young Lee, Nam Heon Cho, Sang Won Im, Hye-Eun Lee, Hyo-Yong Ahn, and Ki Tae Nam. Chiral 432 helicoid ii nanoparticle synthesized with glutathione and poly (t) 20 nucleotide. *ChemNanoMat*, 6(3):362–367, 2020.
- [16] Keng-Te Lin, Han Lin, and Baohua Jia. Plasmonic nanostructures in photodetection, energy conversion and beyond. *Nanophotonics*, 9(10):3135–3163, 2020.
- [17] Stefan A Maier and Harry A Atwater. Plasmonics: Localization and guiding of electromagnetic energy in metal/dielectric structures. *Journal of applied physics*, 98(1):10, 2005.
- [18] Stefan A Maier et al. *Plasmonics: fundamentals and applications*, volume 1. Springer, 2007.
- [19] Stella M Marinakos, Sihai Chen, and Ashutosh Chilkoti. Plasmonic detection of a model analyte in serum by a gold nanorod sensor. *Analytical chemistry*, 79(14):5278–5283, 2007.
- [20] Catherine J Murphy, Tapan K Sau, Anand M Gole, Christopher J Orendorff, Jinxin Gao, Linfeng Gou, Simona E Hunyadi, and Tan Li. Anisotropic metal nanoparticles: synthesis, assembly, and optical applications. *The Journal of Physical Chemistry B*, 109(29):13857–13870, 2005.
- [21] Bing Ni, Mikhail Mychinko, Sergio Gómez-Graña, Jordi Morales-Vidal, Manuel Obelleiro-Liz, Wouter Heyvaert, David Vila-Liarte, Xiaolu Zhuo, Wiebke Albrecht, Guangchao Zheng, et al. Chiral seeded growth of gold nanorods into fourfold twisted nanoparticles with plasmonic optical activity. *Advanced Materials*, 35(1):2208299, 2023.
- [22] Peter N Njoki, I-Im S Lim, Derrick Mott, Hye-Young Park, Bilal Khan, Suprav Mishra, Ravishanker Sujakumar, Jin Luo, and Chuan-Jian Zhong. Size correlation of optical and spectroscopic properties for gold nanoparticles. *The Journal of Physical Chemistry C*, 111(40):14664–14669, 2007.
- [23] Cecilia Noguez. Surface plasmons on metal nanoparticles: the influence of shape and physical environment. *The Journal of Physical Chemistry C*, 111(10):3806–3819, 2007.

- [24] Matthew Pelton and Garnett W Bryant. *Introduction to metal-nanoparticle plasmonics*. John Wiley & Sons, 2013.
- [25] Michelle L Personick and Chad A Mirkin. Making sense of the mayhem behind shape control in the synthesis of gold nanoparticles. *Journal of the American Chemical Society*, 135(49):18238–18247, 2013.
- [26] Jörg Polte. Fundamental growth principles of colloidal metal nanoparticles—a new perspective. *CrystEngComm*, 17(36):6809–6830, 2015.
- [27] Daeha Seo, Ji Chan Park, and Hyunjoon Song. Polyhedral gold nanocrystals with oh symmetry: From octahedra to cubes. *Journal of the American Chemical Society*, 128(46):14863–14870, 2006.
- [28] David S Sholl, Aravind Asthagiri, and Timothy D Power. Naturally chiral metal surfaces as enantiospecific adsorbents, 2001.
- [29] Nguyen TK Thanh, N Maclean, and S Mahiddine. Mechanisms of nucleation and growth of nanoparticles in solution. *Chemical reviews*, 114(15):7610–7630, 2014.
- [30] Hsin-Lun Wu, Chun-Hong Kuo, and Michael H Huang. Seed-mediated synthesis of gold nanocrystals with systematic shape evolution from cubic to trisoctahedral and rhombic dodecahedral structures. *Langmuir*, 26(14):12307–12313, 2010.
- [31] Hsin-Lun Wu, Huei-Ru Tsai, Yun-Ting Hung, Ka-Un Lao, Ching-Wen Liao, Pei-Ju Chung, Jer-Shing Huang, I-Chia Chen, and Michael H Huang. A comparative study of gold nanocubes, octahedra, and rhombic dodecahedra as highly sensitive sers substrates. *Inorganic chemistry*, 50(17):8106–8111, 2011.
- [32] Wenbing Wu and Matthias Pauly. Chiral plasmonic nanostructures: recent advances in their synthesis and applications. *Materials Advances*, 3(1):186–215, 2022.
- [33] Zhaohui Wu, Shuanglei Yang, and Wei Wu. Shape control of inorganic nanoparticles from solution. *Nanoscale*, 8(3):1237–1259, 2016.
- [34] Jin Z Zhang and Cecilia Noguez. Plasmonic optical properties and applications of metal nanostructures. *Plasmonics*, 3:127–150, 2008.
- [35] Lei Zhang and Younan Xia. Scaling up the production of colloidal nanocrystals: should we increase or decrease the reaction volume? *Advanced materials*, 26(16):2600–2606, 2014.